AIAA JOURNAL
Vol. 45, No. 5, May 2007

Ray-Tracing Approach to Calculate Acoustic Shielding by a Flying Wing Airframe

Anurag Agarwal,* Ann P. Dowling,† Ho-Chul Shin,‡ and Will Graham§
University of Cambridge, Cambridge, CB2 1PZ England, United Kingdom
and
Sandy Sefi¶
Royal Institute of Technology (KTH), 100 44 Stockholm, Sweden

DOI: 10.2514/1.26000

The "silent aircraft" is in the form of a flying wing with a large wing planform and a propulsion system that is embedded in the rear of the airframe with intakes on the upper surface of the wing. Thus a large part of the forward-propagating noise from the intake ducts is expected to be shielded from observers on the ground by the wing. Acoustic shielding effects can be calculated by solving an external acoustic scattering problem for a moving aircraft. In this paper, acoustic shielding effects of the silent aircraft airframe are quantified by a ray-tracing method. The dominant frequencies from the noise spectrum of the engines are sufficiently high for ray theory to yield accurate results. It is shown that, for low-Mach number homentropic flows, a condition satisfied approximately during takeoff and approach, the acoustic rays propagate in straight lines. Thus, from Fermat's principle it is clear that classical geometrical optics and geometrical theory of diffraction solutions are applicable to this moving-body problem as well. The total amount of acoustic shielding at an observer located in the shadow region is calculated by adding the contributions from all the diffracted rays (edge-diffracted and creeping rays) and then subtracting the result from the incident field without the airframe. The three-dimensional ray-tracing solver is validated by comparing the numerical solutions with analytical high-frequency asymptotic solutions for canonical shapes. Experiments on a model-scale geometry have been conducted in an anechoic chamber to test the applicability of the ray-tracing technique. The results confirm the accuracy of the approach, which is then applied to a CAD representation of a prototype silent aircraft design. As expected, the flying wing configuration provides very significant ground shielding (in excess of 10 dB at all locations) of a source above the airframe.

I. Introduction

THE "silent aircraft initiative" has a very aggressive goal of reducing aircraft noise to the point where it would be below the background noise outside a typical city airport. Because the silent aircraft is in the form of a flying wing with a large wing planform and a propulsion system that is embedded in the rear of the airframe with intake on the upper surface of the wing, a large part of the forward-propagating noise from the intake duct of the engines is expected to be shielded from observers on the ground by the wing. Acoustic shielding by the wing is essential in achieving the silent aircraft's stringent noise target. In a previous paper [1], we quantified the amount of shielding from low frequency (of the order of the fan shaft frequency) simple sources using boundary element methods. The objective of the present paper is to extend the analysis to calculate the amount of shielding at the higher frequencies that dominate the engine noise spectrum. This is accomplished by using a ray-tracing method. The dominant frequencies from the noise spectrum of the engines are sufficiently high for asymptotic methods to yield accurate results. Mathematically, if we expand an acoustic variable, say pressure, as a power series in inverse powers of frequency ω, then the leading term satisfies the ray theory equations. The solution to these equations is also referred to as the physical optics (PO) solution. Geometrically, these represent direct and reflected rays. However, when there is an obstacle between an acoustic source and observer such that there is no direct line of sight between the source and the observer, that is when the observer is the shadow region, the leading term in the power series expansion vanishes. To account for the acoustic field in the shadow regions the PO solution needs to be extended to include higher-order terms. The geometrical theory of diffraction (GTD) [2] is a powerful technique that provides such an extension. GTD introduces new kinds of rays called diffracted rays that account for the acoustic field in the shadow region. In Sec. II we derive the ray theory equations from first principles and show that for low-Mach number homentropic flows, a condition satisfied approximately by the silent aircraft during takeoff and approach, the acoustic rays propagate in a straight line. Thus, from Fermat's principle it is clear that classical geometrical optics and geometrical theory of diffraction solutions are applicable to this moving-body problem as well. There are two types of diffracted rays, creeping and sharp-edge diffracted rays. A brief description of the diffracted rays and their associated acoustic fields is given in Sec. III. There are several advantages of using a geometrical ray theory approach. Because the method is geometric, computationally, it is not dependent on the size of the geometry, only its complexity. Furthermore there is no added penalty for higher frequencies. The rays need to be traced only once to compute the acoustic field for multiple frequencies. The ray-tracing technique is not memory intensive and is amenable to a parallel implementation. Perhaps the biggest advantage of this technique is that it provides a visual interpretation for sound at any location. We have used an object-oriented ray-tracing simulator called MIRA [3] based on Fermat's

Presented as Paper 2618 at the 12th AIAA/CEAS Aeroacoustics Conference (27th AIAA Aeroacoustics Conference), Cambridge, Massachusetts, 8–10 May 2006; received 22 June 2006; revision received 20 December 2006; accepted for publication 23 December 2006.

*Research Associate, Department of Engineering. Present Address: Institute of Sound and Vibration Research, University Road, Southampton SO17 1BJ. Member AIAA.

†Professor of Mechanical Engineering and Head of Energy, Fluid Mechanics and Turbomachinery Division. Member AIAA.

‡Research Associate, Department of Engineering. Member AIAA.

§Senior Lecturer, Department of Engineering.

¶Ph.D. Student, Department of Numerical Analysis and Computer Science, School of Computer Science and Communication.

principle that works on complex geometries. The geometry is described by NURBS (nonuniform rational B spline) and rational Bezier patches. NURBS is a standard for parametric surface representation. MIRA was originally developed as a part of the Swedish code development project GEMS (general electromagnetic solvers) for electromagnetic applications. A brief description of the geometry input and the calculation of the diffracted rays by MIRA is provided in Sec. IV. The three-dimensional ray-tracing solver is validated by comparing the numerical solutions with analytical high-frequency asymptotic solutions for canonical shapes in Sec. V. The applicability of the ray-tracing technique is tested by comparing the simulated results with experimental results for a scaled model planform. The details of the experimental setup and comparisons with numerical solutions are presented in Sec. VI. Numerical calculations for a three-dimensional silent aircraft airframe are presented in Sec. VII.

II. Ray Theory

Acoustic shielding effects can be calculated by solving an external acoustic scattering problem. Acoustic waves generated by the engines are refracted by the mean flow past the moving aircraft. For low-Mach number homentropic flows, such as high Reynolds number flows past slender bodies moving parallel to their length, significant simplifications can be made to the problem of acoustic ray tracing through an ambient flowfield.

For a constant frequency disturbance, let the wave fronts of the ensuing acoustic waves be described by $\tau(\boldsymbol{x}_p) = t$, where $\boldsymbol{x}_p$ is a locus of points on the wave front at time t. Let $\boldsymbol{n}$ be the unit-normal vector at a point $\boldsymbol{x}$ on the wave front as shown in Fig. 1. Since $\nabla\tau$ is parallel to $\boldsymbol{n}$,

$$\boldsymbol{n} = \nabla\tau/|\nabla\tau| \tag{1}$$

Let a ray be denoted by the parametric curve $\boldsymbol{\sigma} = \boldsymbol{\sigma}(s)$, where s is the distance along the ray. A wave front moves in a direction normal to itself at the local speed of sound c while being convected by the local mean flow $\bar{\boldsymbol{u}}$. Thus, for a ray to follow a wave front, its velocity at any instant should be given by [4]

$$\frac{\mathrm{d}\boldsymbol{\sigma}}{\mathrm{d}t} = c\boldsymbol{n}(\boldsymbol{x}) + \bar{\boldsymbol{u}}(\boldsymbol{x}) \tag{2}$$

Thus the tangent to the ray $(\mathrm{d}\boldsymbol{\sigma}/\mathrm{d}s)$ must be parallel to $c\boldsymbol{n}(\boldsymbol{x}) + \bar{\boldsymbol{u}}(\boldsymbol{x})$. This can be written as

$$\frac{\mathrm{d}\boldsymbol{\sigma}}{\mathrm{d}s} = \alpha[c\boldsymbol{n}(\boldsymbol{x}) + \bar{\boldsymbol{u}}(\boldsymbol{x})] \tag{3}$$

where α is a scalar. Since $|\mathrm{d}\boldsymbol{\sigma}/\mathrm{d}s|$ is unity,

$$\frac{\mathrm{d}\boldsymbol{\sigma}}{\mathrm{d}s} = (c\boldsymbol{n} + \bar{\boldsymbol{u}})/|c\boldsymbol{n} + \bar{\boldsymbol{u}}| \tag{4}$$

Using Eq. (1) and defining the local Mach number as $\boldsymbol{M} = \bar{\boldsymbol{u}}/c$, Eq. (4) can be written as

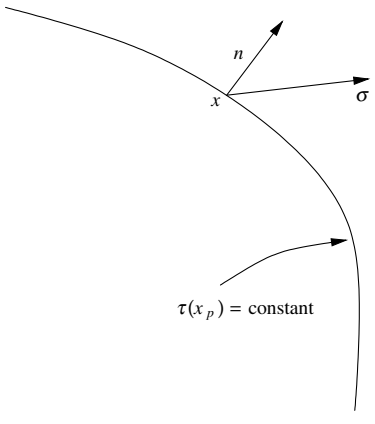

Fig. 1 Schematic of a wave front and a ray.

$$\frac{\mathrm{d}\boldsymbol{\sigma}}{\mathrm{d}s} = \left(\frac{\nabla\tau}{|\nabla\tau|} + \boldsymbol{M}\right)\left[\left(\frac{\nabla\tau}{|\nabla\tau|} + \boldsymbol{M}\right)\cdot\left(\frac{\nabla\tau}{|\nabla\tau|} + \boldsymbol{M}\right)\right]^{-1/2} \tag{5}$$

After neglecting terms of order M^2 in comparison with those of order unity, Eq. (5) reduces to

$$\frac{\mathrm{d}\boldsymbol{\sigma}}{\mathrm{d}s} = \frac{\nabla\tau}{|\nabla\tau|} - \frac{\nabla\tau(\nabla\tau\cdot\boldsymbol{M})}{|\nabla\tau|^2} + \boldsymbol{M} \tag{6}$$

To proceed further, an expression for $|\nabla\tau|$ is required. This is given by the *eikonal equation* [4]

$$|\nabla\tau| = \frac{1}{c} - \nabla\tau\cdot\boldsymbol{M} \tag{7}$$

Using Eq. (7), and neglecting terms of order M^2, Eq. (6) can be written after some manipulations as

$$\frac{\mathrm{d}\boldsymbol{\sigma}}{\mathrm{d}s} = c\nabla\tau + \boldsymbol{M} \tag{8}$$

For a potential flow, $\boldsymbol{M} = \nabla\bar{\phi}/c$. Hence,

$$\frac{\mathrm{d}\boldsymbol{\sigma}}{\mathrm{d}s} = \nabla(c\tau + \bar{\phi}/c) \tag{9}$$

Using the transformation

$$T = \tau + \bar{\phi}/c^2 \tag{10}$$

Eq. (9) reduces to

$$\frac{\mathrm{d}\boldsymbol{\sigma}}{\mathrm{d}s} = c\nabla T \tag{11}$$

Equation (10) is the same as Taylor's transformation [5]. Interestingly, it is a natural choice for the transformation of coordinates to simplify the analysis. The transformation changes the arrival time of a wave front at a point $\boldsymbol{x}$ by $\bar{\phi}(\boldsymbol{x})/c^2$. The direction of the rays is unaffected by this transformation. Using this transformation, and neglecting terms of order M^2, the eikonal equation reduces to

$$|\nabla T| = 1/c \tag{12}$$

the form in the absence of a mean flow. It is clear from Eq. (11) that the transformed wave front $T(\boldsymbol{x}) = \text{const}$ is perpendicular to the rays $(\boldsymbol{\sigma})$. Thus,

$$\frac{\mathrm{d}}{\mathrm{d}s}\left(\frac{1}{c}\frac{\mathrm{d}\boldsymbol{\sigma}}{\mathrm{d}s}\right) = \left(\frac{\nabla T}{|\nabla T|}\cdot\nabla\right)\frac{\mathrm{d}\boldsymbol{\sigma}}{\mathrm{d}s} = c(\nabla T\cdot\nabla)\nabla T \tag{13}$$

Using the vector identity

$$(\boldsymbol{A}\cdot\nabla)\boldsymbol{A} = \tfrac{1}{2}\nabla|\boldsymbol{A}|^2 + (\nabla\times\boldsymbol{A})\times\boldsymbol{A} \tag{14}$$

Eq. (13) can be written as

$$\frac{\mathrm{d}}{\mathrm{d}s}\left(\frac{1}{c}\frac{\mathrm{d}\boldsymbol{\sigma}}{\mathrm{d}s}\right) = \nabla\left(\frac{1}{c}\right) \tag{15}$$

For a homogeneous medium,

$$\frac{\mathrm{d}}{\mathrm{d}s}\left(\frac{\mathrm{d}\boldsymbol{\sigma}}{\mathrm{d}s}\right) = 0 \tag{16}$$

which means that the rays are straight lines. This result can also be obtained directly from Eq. (9) and the eikonal equation (7). Thus for low-Mach-number homentropic potential flows, acoustic rays are straight lines and hence the propagation medium can be treated as homogeneous. This result has some interesting physical implications. From Fermat's principle it follows that classical geometrical optics and GTD solutions are applicable to this moving-body problem as well. Jeffery and Holbeche [6] made acoustic wind-tunnel measurements by mounting an acoustic monopole source

above a delta wing. For low angles of attack, they observed that the shadow-zone boundaries below the wing remained unchanged with variations in flow speeds at low Mach numbers. This result is explained easily for linear acoustic rays. Also, the adjoint solution to the sound propagation problem can be found easily; for the source and observer locations can be exchanged to yield the same solution as for the direct problem if the time delay in Eq. (10) is switched to a time lead, that is, if $\bar{\phi}$ is replaced with $-\bar{\phi}$.

The magnitude of the acoustic pressure in general depends on the characteristics of the source. Consider a time-harmonic point source for the convected wave equation. The Taylor's transformation only changes the arrival time of the rays at an observer location. With respect to the transformed time (T), Eqs. (12) and (16) represent sound propagation in a homogeneous and isotropic medium. The acoustic potential along a ray in such a medium is well known and is given by [7]

$$\phi \propto \frac{\exp[ikr]}{r} \tag{17}$$

where $r = |\boldsymbol{x} - \boldsymbol{x}_o|$ is the distance from the source at $\boldsymbol{x}_o$ along a ray. The amplitude of the acoustic potential at any point is unaffected by the mean flow. However, because the arrival time is changed by the Taylor's transformation, the mean flow shifts the phase by a factor of $\omega\bar{\phi}(\boldsymbol{x})/c^2$. Thus the acoustic potential with the background flow is given by

$$\phi(\boldsymbol{x}, t) \propto \frac{\exp(ikr)}{r}\exp\{-i\omega[t + (\bar{\phi}(\boldsymbol{x}) - \bar{\phi}(\boldsymbol{x}_o))/c^2]\} \tag{18}$$

Note that the acoustic pressure is given by the Bernoulli equation and both its magnitude and phase are affected by the mean flow.

III. Geometrical Theory of Diffraction

The GTD is an extension of physical (geometrical) optics which is based on the postulate that at high frequencies (large $ka = 2\pi a/\lambda$, where a is the object dimension and λ is the wavelength) wave fields are governed by local conditions and they propagate along rays. A physical optics solution fails to account for the diffracted field in a shadow region where there is no direct line of sight between the source and the receiver. GTD introduces a new kind of rays called diffracted rays that contribute to the field value in the shadow region. There are two kinds of diffracted rays—edge-diffracted rays and creeping rays. Edge-diffracted rays are produced when a ray is incident on a sharp edge or corner. Creeping rays are produced when a ray is incident on an object at a grazing incidence. The ray then lies in part on the surface, creeps along the surface, and leaves it at a grazing angle to the observer. Note that away from the surface these rays behave as ordinary rays. A description of the fields for direct and diffracted rays is given in the following sections.

A. Direct Field

In a homogeneous medium rays are straight lines. Consider a straight ray from P to Q with a time dependence of $\exp(-i\omega t)$ and a wave number of $k = \omega/c$. Let s be the distance between P and Q, then the field at Q is given by

$$\phi(Q) = \phi(P)\left[\frac{\rho_1\rho_2}{(\rho_1 + s)(\rho_2 + s)}\right]^{1/2} e^{iks} \tag{19}$$

where $\phi(P)$ is the field at P and ρ_1, ρ_2 are the principal radii of curvature of the wave front through P. It can be shown that for a point source this expression takes the form in Eq. (17).

B. Edge-Diffracted Field

The edge-diffracted ray is given by Fermat's principle of edge diffraction: The edge-diffracted ray path from a source at point P to a receiver at point Q has a stationary length of the paths from P to Q with a point on the edge. For a homogeneous medium this means that the incident and diffracted rays make equal angles with the edge (θ_o) at the point of diffraction (Q_e) and lie on opposite sides of the plane normal to the edge. This leads to a cone of diffracted rays as shown in Fig. 2. The vertex of the cone coincides with the diffraction point (Q_e) and its axis is aligned with the edge. The edge-diffracted field is given by [2]

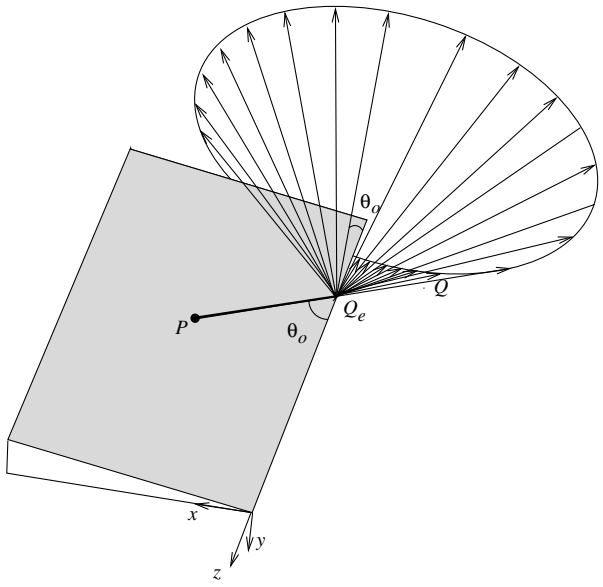

Fig. 2 A ray incident on a sharp edge diffracts into a cone of rays. The axis of the cone is aligned with the edge.

$$\phi(P) = \phi^i(Q_e)D\sqrt{\frac{\rho}{s(s+\rho)}}e^{iks} \tag{20}$$

Note that the edge itself is a caustic so that ρ actually is the second caustic distance that depends on the radius of curvature of the edge at Q_e. Here $\phi^i(Q_e)$ is the incident field at Q_e and D is the diffraction coefficient given by [2]

$$D = \frac{\exp(-i\pi/4)\nu\sin(\nu\pi)}{\sqrt{2\pi k}\sin\gamma}\left[\frac{1}{\cos\nu\pi - \cos\nu(\phi - \phi_s)} + \frac{1}{\cos\nu\pi - \cos\nu(\phi + \phi_s)}\right] \tag{21}$$

where γ is the oblique angle between the incident ray and the edge, and $\nu = \pi/\beta$ is the wedge index. The other parameters are defined in Fig. 3. Note that the diffracted field is inversely proportional to a square root of frequency. Thus for an edge-diffracted field doubling the frequency reduces the sound field by approximately 3 dB.

C. Creeping Field

Diffracted rays around a smooth object can be characterized by an extended form of Fermat's principle: In traveling from a source point P to an observer point Q (see Fig. 4), the surface diffracted ray path is such as to make the total distance from P to Q an extremum. From

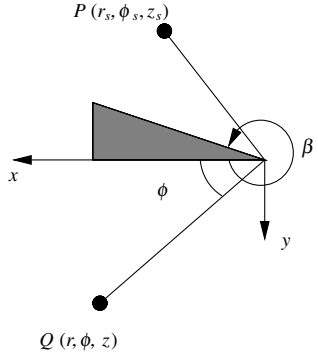

Fig. 3 Parameters for diffraction from a sharp edge.

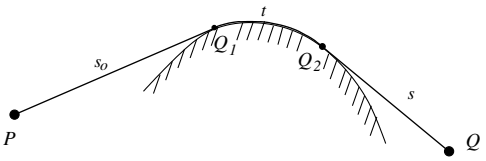

Fig. 4 Diffraction of a single ray from P to Q around a curved surface. The ray consists of a straight line segment tangent to the surface at Q_1, a geodesic arc of length t on the surface from Q_1 to Q_2, and a straight line segment from the tangent point Q_2 to Q.

this it follows that PQ_1 and Q_2Q are straight lines tangent at Q_1 and Q_2, respectively, and Q_1Q_2 is a geodesic arc along the surface.

The creeping-ray field is given by [8]

$$\phi(Q) = \phi^i(Q_1)T(Q_1, Q_2)\sqrt{\frac{\rho}{s(\rho + s)}}e^{iks} \tag{22}$$

where $T(Q_1, Q_2)$ is a transfer function that relates the diffracted field at Q_2 to the incident field at Q_1:

$$T(Q_1, Q_2) = \sum_m D_m(Q_1)\left[\exp\left(ikt - \int_0^t \alpha_m(\tau)\,\mathrm{d}\tau\right)\sqrt{\frac{\mathrm{d}\sigma(Q_1)}{\mathrm{d}\sigma(Q_2)}}\right]D_m(Q_2) \tag{23}$$

where $D_m(Q)$ is the diffraction coefficient at Q that depends on k and the local property of the geometry, t is the geodesic length, α_m is the decay coefficient, and the ratio $[\mathrm{d}\sigma(Q_1)/\mathrm{d}\sigma(Q_2)]^{1/2}$ represents the attenuation of the creeping-ray field due to the divergence of two nearby creeping rays from the point of attachment (Q_1) to the point of exit (Q_2). For a cylindrical field nearby rays would not diverge and hence this ratio would be unity. The decay coefficients α_m depend on the frequency and the local properties of the surface. It can be seen from Eq. (23) that the creeping-ray field decays exponentially with increasing creeping length. This is because a creeping ray continuously sheds rays as it travels along the surface.

IV. Ray-Tracing Program

In this section, we describe briefly how the geometry is used as input for the numerical simulator and how the edge-diffracted and creeping rays are calculated. For details see [9]. The three-dimensional objects with which the rays interact are made up of a collection of large smooth parametric surfaces subdivided into a combination of patches. The set of patches form a complete skin representing the solid with no missing parts. Mathematically, the surfaces are modeled by a NURBS and rational Bezier surfaces trimmed with bounding curves. Such a representation is a standard used by the CAD industry to represent complex free-form geometries. Internally, the software handles the NURBS surfaces by converting them into rational Bezier patches. Each patch is bounded (trimmed) by 2-D curves in the parametric domain of definition of the surface. Each curve is represented by a set of edges that can be segments or Bezier curves.

The edge-diffracted rays are calculated by finding the extremum of the total distance from the source to an edge and from the edge to the receiver. This is done by using a conjugate gradient method. Because a polynomial functional form is available for the edge, this extremum can be obtained to an arbitrary precision.

Creeping-ray calculations are a little more complicated. Because a creeping ray arrives and leaves a curved surface at tangent points, the first step is to find the shadow line for a set of sampling points. The shadow line is a locus of tangent points from the source to the curved surface. For each sample point on the shadow line we trace the geodesic curve and cross over the ray between two surfaces if needed. The determination of geodesics is a problem of differential geometry. Geodesics on a parametric surface can be found as a solution of the geodesic equations, a set of nonlinear ordinary differential equations. The final step in the creeping-ray tracing is to exit the surface at the receiver shadow line. Because the method works on a discrete sampling of the shadow curve, the solution is approximate. The error is controlled by the density of the sampling points.

V. Diffraction by a Circular Cylinder

The creeping-ray solver is validated by solving the three-dimensional problem of diffraction of acoustic waves by a circular cylinder. Consider a circular cylinder of radius a with its generators parallel to the z axis. Let a point (monopole) acoustic source ($ka = 100$, k being the wave number) be located at $P(2a, \pi/2, 0)$ in a (r, θ, z) cylindrical polar coordinate system (Fig. 5). Consider observers located along the arc $(2a, -\pi/3 \le \theta \le -5\pi/6, a)$. Figure 5a shows the location of one such observer. It can be seen that there are two rays emanating from the source P that creep (diffract) around the cylinder to an observer Q. It can be shown that the creeping rays trace a helical path around the cylinder (see the Appendix). Actually there are an infinite family of rays from P to Q (with different pitch angles) that wrap around the cylinder multiple times. Because the creeping-ray field decays exponentially with increasing creeping length, these other rays that wrap around the cylinder more than once will have negligible field strength by the time they reach the observer and are hence neglected. The total acoustic field at an observer location is then the sum of the pressure fields from the two rays. Figure 6 shows the root-mean-square pressure field for the various observer locations. Also shown is the analytical solution (see the Appendix) at these locations. It can be seen that the numerical solution is in good agreement with the analytical solution.

The sharp-edge diffraction solver has been validated by comparing the diffraction field from a wedge like the one shown in Fig. 3 with the analytical solution given by Eq. (20).

VI. Diffraction by a Thin Wing

A. Experimental Setup

To test the applicability of the ray-tracing technique we carried out some experiments in an anechoic chamber at the Cambridge University Engineering Department. Figure 7 shows a photograph of the experimental setup. As a sound source, a compression driver is extended by a pipe to simulate a point source at its exit. The inner diameter of the pipe is about 16 mm and its length is approximately 1 m. It is supported by three retort stands, two of which hold the driver, and the third supports the pipe. The pipe, compression driver, and retort stands are covered by plastic foam. The directivity pattern of the source at the exit of the pipe is evaluated by measuring the sound field at a fixed radial distance. The results show that the compression driver and pipe system has a near-uniform directivity for frequencies up to 4 kHz in both magnitude and phase. Hence, up to 4 kHz, this noise source can be regarded as a monopole.

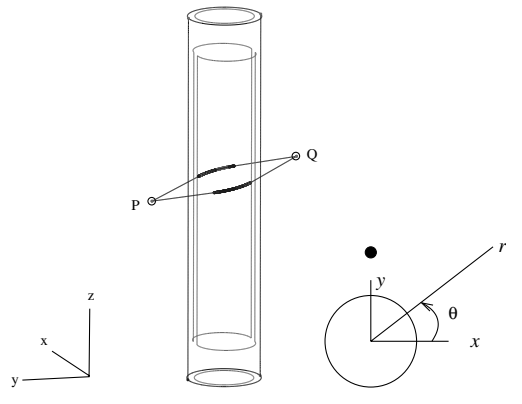

Fig. 5 Two rays emanating from a monopole acoustic source at P ($ka = 100$) creep around a cylinder of radius a to a point Q.

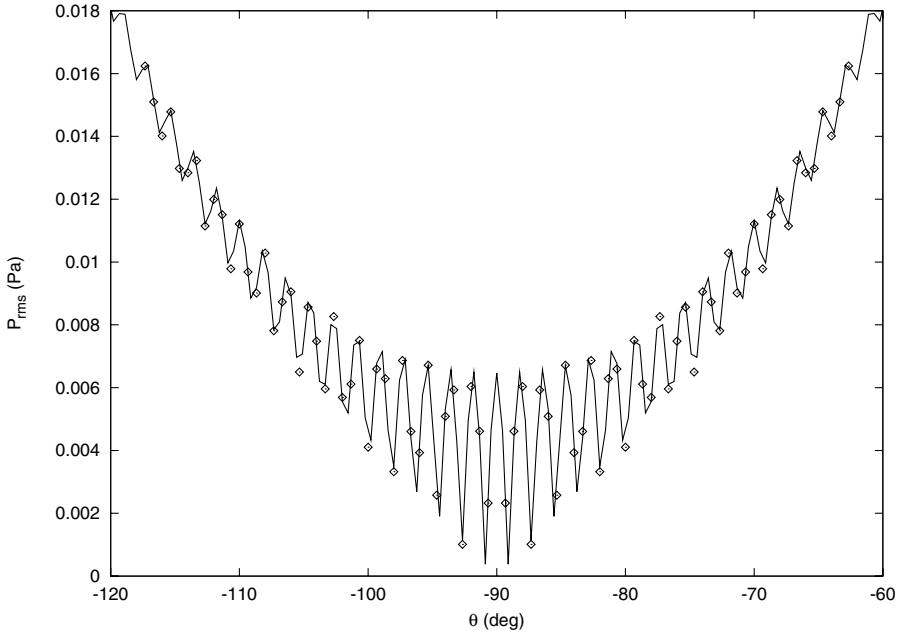

Fig. 6 Comparison between the root-mean-square pressures computed by a creeping-ray solver (diamond) and the analytical solution (solid line).

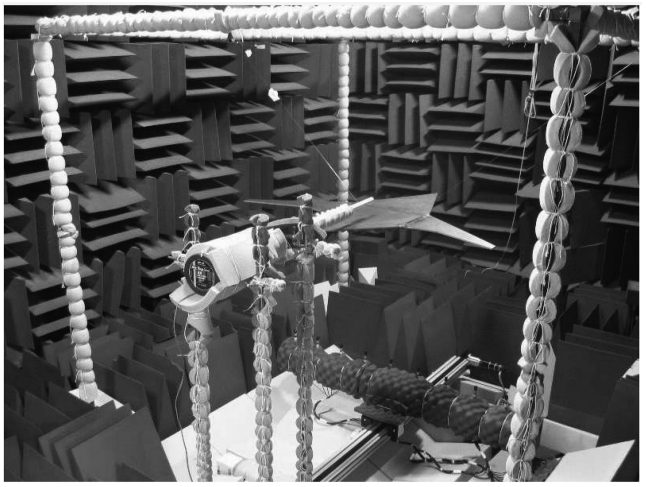

Fig. 7 A photograph of the experimental setup in an anechoic chamber.

The main shielding measurements have been conducted with a nearly two-dimensional planform model (Fig. 8) and subsequently without it under the same configuration of the sound source and microphones. The planform is a 1/50 scaled model of a silent aircraft design (designated SAX10 [10]) made out of steel. Its chord length, span, and thickness are 0.92 m, 1.17 m, and 5 mm, respectively. The model is suspended by three wires from a (2 m × 2 m × 2 m) metal frame, wrapped with plastic foam for acoustic absorption. The exit of the pipe (source) is located 60 cm from the leading edge on the central chord line, and its center is positioned 6.5 cm above the planform.

A microphone traverse system is used to survey the sound field for shielding experiments. A line of microphones mounted on a frame along the *Y* axis (spanwise direction) is moved along the *X* axis on a belt driven by a dc motor. The motor is controlled by a PC outside the anechoic chamber. For the experimental results reported in this paper, sound fields were recorded every 2.5 cm along the *X* axis. The planform was located 1.12 m above the microphones.

Band-limited white noise is created by a noise generator and is further filtered by a bandpass filter between 500 Hz to 20 kHz. The electrical signal is then amplified and fed to the compression driver. The signal is relayed to a data acquisition system and then serves as a reference for acoustic signals from microphones, to take into account different source strengths between measurement sessions. Sound pressures are captured by prepolarized condenser microphones with preamplifiers, whose signal is further amplified and filtered by an antialiasing filter. Finally, they are digitized with 16-bit resolution at a sampling frequency of 65.5 kHz by a data logger with a multichannel simultaneous sample-and-hold capability. In post-processing the time-domain signals are transformed to the frequency domain by an fast Fourier transform (FFT) algorithm. During the frequency analysis, a Hanning window is applied to the FFT blocks of data, which are then overlapped and averaged. Transfer functions are calculated between the acoustic signals and the reference source signal. To quantify the amount of shielding achieved by the planform, the insertion loss at each measurement location is evaluated between the magnitudes of transfer functions with and without the planform.

B. Comparison with Numerical Solution

For the numerical solution, we placed a monopole point source at 0.6, 0, 0.065 m. Figure 9 shows the edge-diffracted rays at various observers located along the line $y = 0.675$ m. Each observer receives rays diffracted from multiple edges. The locations of the intersections of the rays with the edges are computed automatically

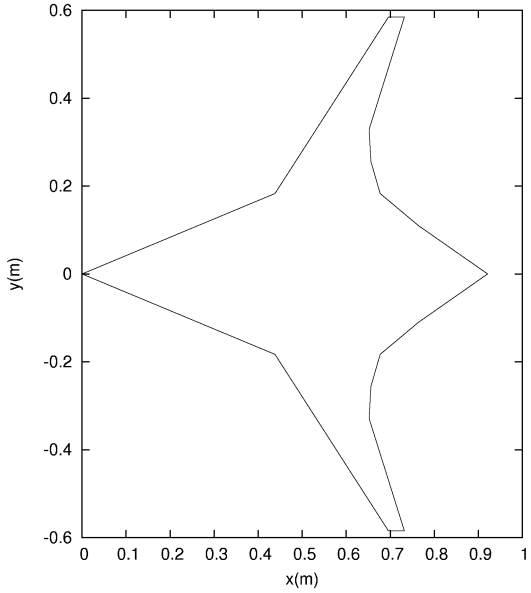

Fig. 8 Scaled (1/50) model of the silent aircraft (SAX10) design.

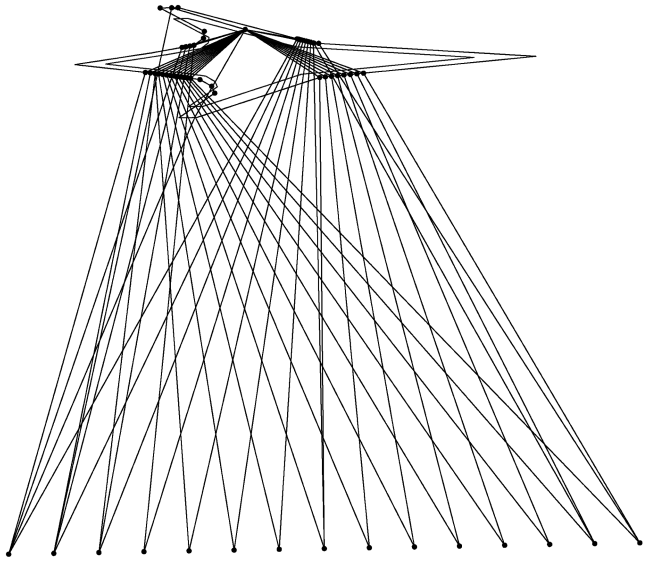

Fig. 9 Acoustic rays emanating from a monopole source above a thin planform diffract around the sharp edges to reach the observers in the shadow region underneath the wing.

by a conjugate gradient solver as explained in Sec. IV. The total field at each location is a sum of the fields from all the rays. This leads to an interference pattern as shown in Fig. 10. The source frequency for this case is 2500 Hz. This figure compares the numerical solution at $y = \pm 0.675$ m with the experimental solution. The solution should ideally be symmetric about $y = 0$. The experimental result is slightly asymmetric because of the inherent experimental error. The numerical solution compares very well with the experimental solution. Similar agreements can be found at other locations and frequencies. For example, Fig. 11 shows the corresponding comparisons at 4000 Hz and Fig. 12 shows a comparison along $y = 0.375$ at 2500 Hz. The numerical solution exhibits sharp discontinuities in slope at certain x locations. This can be explained by the following argument. The edges of this wing are piecewise linear and there is a discontinuity in slope where they meet the neighboring edges (at corners). This leads to a discontinuous distribution of rays (the diffraction cone axis for two neighboring edges are different). Thus we see a discontinuity in the acoustic field in the vicinity of an observer that receives a diffracted ray from near the end points of an edge (corner). The diffraction field from the corners is a higher-order effect and is not accounted for in the present numerical simulation. Even though the corner contribution would be negligible in the far field compared with edge diffraction, its effect is to smoothen out the slope discontinuities in the diffracted field as seen in the experimental results.

VII. Acoustic Shielding by a Silent Aircraft

Acoustic shielding effects are estimated by means of a monopole point source placed above the airframe of silent aircraft design SAX20 [11]. Figure 13 shows the orthographic projections of the SAX20 airframe. The source is located at $(0.8a, 0, 0.125a)$, where a is the centerbody chord length.

Figure 14 shows the creeping and sharp-edge diffracted rays from the source to two observer locations. Each observer receives several rays. For example, the observer on the right receives two creeping rays and three edge-diffracted rays, two from the trailing edges and one from the winglet. This leads to a complex interference pattern. For example, Fig. 15 shows the root-mean-square far-field pressures p_{rms} at polar angles between -150 and -30 deg. The total p_{rms} is shown for two source frequencies: 100 and 1000 Hz. Also shown in the figure is the field in the absence of shielding and the creeping and edge-diffracted contributions at 1000 Hz. It is clear that we get a significant amount of shielding at both frequencies. As expected, the total diffracted field at 1000 Hz is lower than that for 100 Hz. Another interesting feature is that the creeping field decays more rapidly than the edge-diffracted field. This is because the creeping-ray field decays exponentially, as a cube root of frequency [see the Appendix, Eq. (A39)] and creeping (geodesic) length.

Figure 16 shows the shielding contour levels for the overall sound pressure levels (OASPL) on the ground, 100 ft below the aircraft. The contour levels represent the difference between the shielded and the unshielded acoustic fields for a source whose amplitude is independent of frequency over the range of 200 to 10,000 Hz. The accuracy of ray theory increases with frequency. But even at the lower end of this frequency range, the size of the airframe is large compared with the acoustic wavelength. Hence ray tracing is expected to provide reasonably accurate results. The negative levels in Fig. 16 indicate the amount of shielding. We obtain at least 10 dB of shielding. The amount is actually higher at most locations except for two diagonal patches near the winglet. We get less shielding at these locations because observers here receive multiple diffracted rays from the winglet. This suggests that we should perhaps use absorbent acoustic liners on the winglet. The actual amount of shielding for the silent aircraft engines would be more effective than

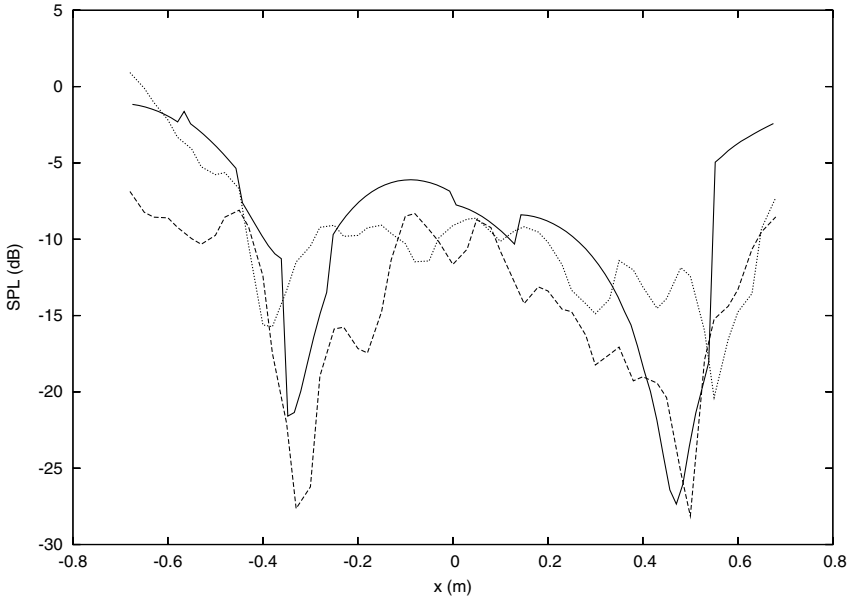

Fig. 10 Comparison of the numerical solution at $y = 0.675$ (solid line) with the experimental solution [$y = 0.675$ (dashed line), $y = -0.675$ (dotted line)]. The source frequency is 2500 Hz.

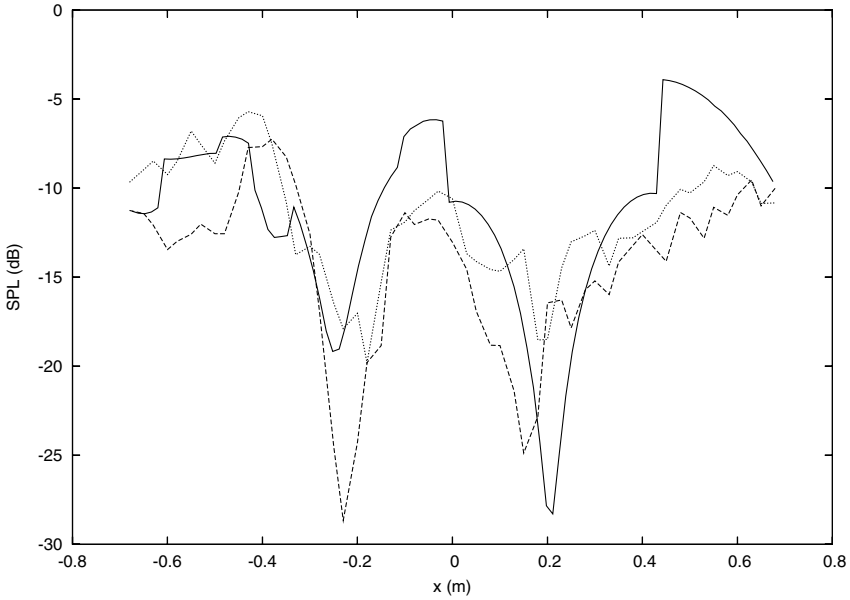

Fig. 11 Same as Fig. 10 but frequency = 4000 Hz.

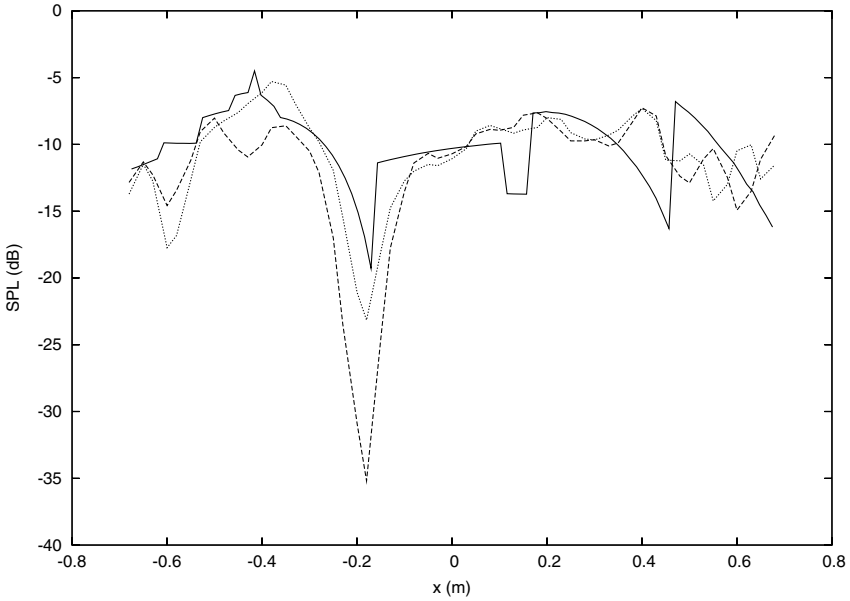

Fig. 12 Comparison of the numerical solution at $y = 0.375$ (solid line) with the experimental solution [$y = 0.375$ (dashed line), $y = -0.375$ (dotted line)]. The source frequency is 2500 Hz.

the levels indicated in this contour plot. This is because the dominant frequencies from the noise spectrum of the engines are high, where shielding is more effective. The effect of lower frequencies, where shielding is less effective, is further reduced by the application of A weighting to calculate perceived noise levels.

As noted in Sec. II, we have neglected the effect of boundary layers on ray propagation. Since the creeping rays creep around the leading edge of the wing, where the boundary-layer thickness is very thin, we expect that the boundary layer would have a small effect on the creeping field. The boundary layer could, however, have a larger impact on the trailing-edge diffracted rays because its thickness is much larger near the trailing edge. A detailed analysis of the effect of boundary layers on diffracted rays could be a subject of future research work.

VIII. Conclusions

The objective of this paper is to apply ray-tracing techniques to predict acoustic shielding of engine noise by the airframe of a silent aircraft during takeoff and approach. Classical ray-tracing techniques are also applicable to moving-body problems, provided the flow past the body has a low Mach number and is potential. Under these conditions the acoustic rays are straight lines. The favorable comparison of our ray-tracing solution with the experimental results for a model scaled planform leads us to conclude that ray tracing is an accurate tool for calculating the diffraction field in the shadow regions. Note that, in general, this is true only if the size of the scattering object is much larger than the acoustic wavelength. Because all the rays to particular observers can be tracked graphically, ray tracing tells us where the sound comes from, thus providing valuable physical insight. For example, for the silent aircraft airframe we observed that a few observer locations were less shielded than most others. Based on the ray traces, we observed that at these locations the winglet was diffracting multiple rays from the source, so we could isolate the problem. Ray tracing has some other advantages as detailed in the Introduction. It does have some disadvantages: It is an approximate method restricted to high frequencies. For high-speed or nonpotential flows the rays would no

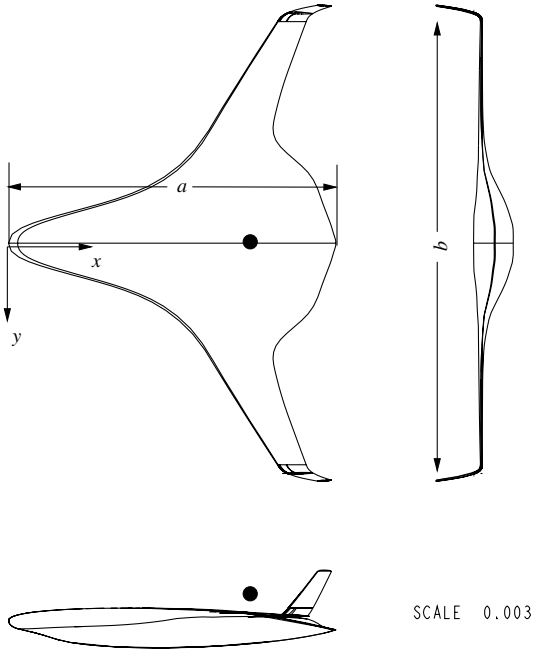

Fig. 13 Orthographic projections of the silent aircraft airframe SAX20.

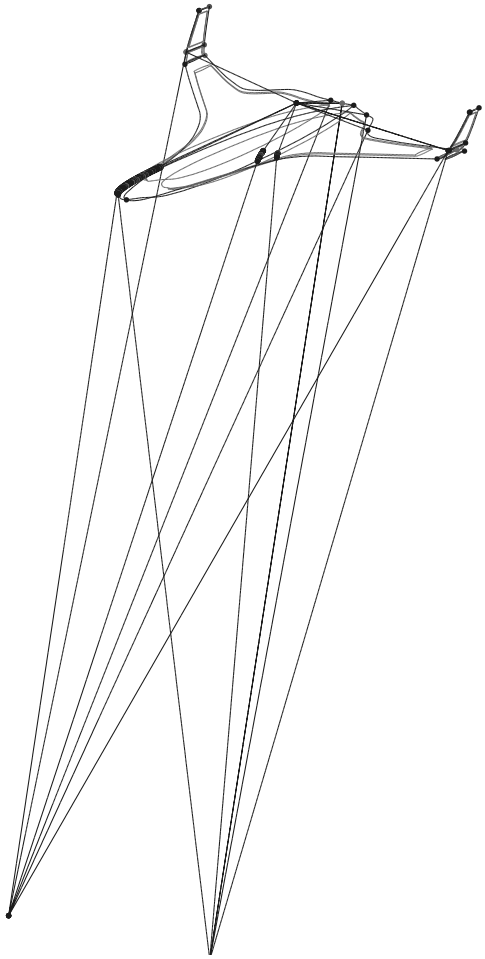

Fig. 14 Creeping and edge-diffracted rays from a monopole acoustic source above the SAX20 airframe to two observers in the shadow region below the airframe.

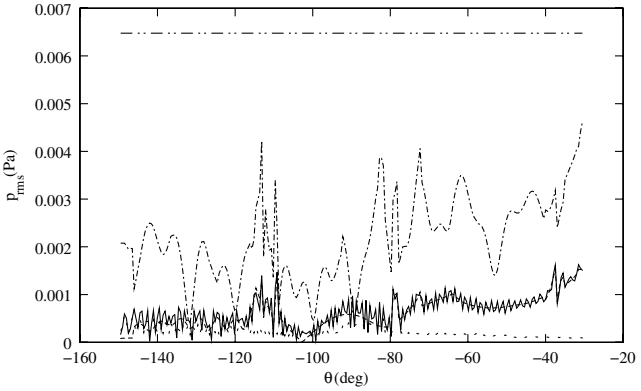

Fig. 15 Root-mean-square far-field pressures as a function of polar angles. Dash-dot-dotted line: incident field; dash-dotted line: total field at 100 Hz; solid line: total field at 1000 Hz; dotted line: creeping-ray field at 1000 Hz; dashed line: sharp edge-diffracted field at 1000 Hz.

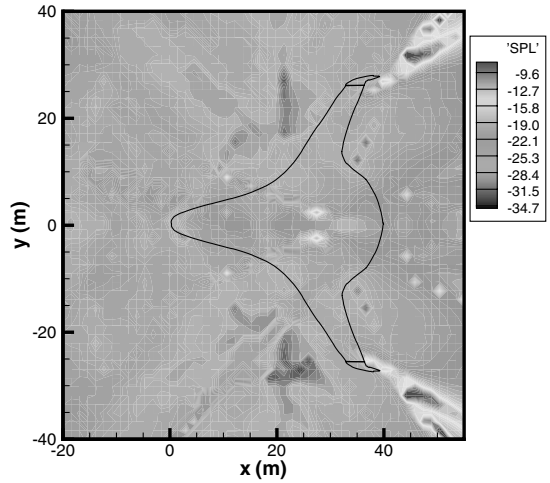

Fig. 16 Shielding contour levels on the ground for SAX20 at a height of 100 ft.

longer be straight lines and they would have to be traced by solving an ordinary differential equation, thus making the technique more complex and less efficient.

Appendix: High-Frequency Asymptotic Solution for the Diffracted Field from a Point Source by a Circular Cylinder

Let us consider the diffraction of an acoustic wave from a point source by a cylinder of radius a. Let the source be located at (ρ_o, ϕ_o, z_o) in a (ρ, ϕ, z) cylindrical polar coordinate system. The axis of the cylinder is aligned with the z axis. The Green's function for this problem satisfies the Helmholtz equation:

$$\left[\frac{\partial^2}{\partial z^2} + \frac{1}{\rho}\frac{\partial}{\partial \rho}\left(\rho\frac{\partial}{\partial \rho}\right) + \frac{1}{\rho^2}\frac{\partial^2}{\partial \phi^2} + k^2\right] g(\boldsymbol{r} \mid \boldsymbol{r_o}; k) = -\frac{4\pi}{\rho}\delta(\rho - \rho_o)\delta(\phi - \phi_o)\delta(z - z_o) \tag{A1}$$

Defining the Fourier transform as

$$G(\zeta) = \int_{-\infty}^{\infty} g(z) e^{-i\zeta(z - z_o)}\, \mathrm{d}(z - z_o) \tag{A2}$$

Equation (A1) transforms into

$$\left[\frac{1}{\rho}\frac{\partial}{\partial\rho}\left(\rho\frac{\partial}{\partial\rho}\right)+\frac{1}{\rho^2}\frac{\partial^2}{\partial\phi^2}+(k^2-\zeta^2)\right]G = -\frac{4\pi}{\rho}\delta(\rho-\rho_o)\delta(\phi-\phi_o) \tag{A3}$$

Let $k^2-\zeta^2=\beta^2$. We now have a two-dimensional problem:

$$(\nabla^2+\beta^2)g(\boldsymbol{r}\mid\boldsymbol{r_o};\beta) = -\frac{4\pi}{\rho}\delta(\rho-\rho_o)\delta(\phi-\phi_o) \tag{A4}$$

The z dependence can be obtained by applying the inverse Fourier transform to the solution of this problem. The incident field from the point source can be expanded in terms of a series in cylindrical coordinates (Morse and Feshbach [12], p. 827)

$$g^I(\boldsymbol{r}\mid\boldsymbol{r_o};\beta) = i\pi H_0^{(1)}(\beta R) = \pi i\sum_{m=0}^{\infty}\epsilon_m\cos[m(\phi x-\phi_o)]\begin{cases} J_m(\beta\rho)H_m^{(1)}(\beta\rho_o); & \rho<\rho_o \\ J_m(\beta\rho_o)H_m^{(1)}(\beta\rho); & \rho>\rho_o\end{cases} \tag{A5}$$

$$\left.\frac{\partial g^I}{\partial\rho}\right|_{\rho=a} = i\pi\beta\sum_{m=0}^{\infty}\epsilon_m\cos[m(\phi-\phi_o)]J_m'(\beta a)H_m^{(1)}(\beta\rho_o) \tag{A6}$$

$$\epsilon_m = \begin{cases}1; & m=0\\ 2; & m>0\end{cases} \tag{A7}$$

Let the scattered field be given by

$$g^s(\boldsymbol{r}\mid\boldsymbol{r_o};\beta) = \sum_{m=0}^{\infty}A_m\cos[m(\phi-\phi_o)]H_m^{(1)}(\beta\rho) \tag{A8}$$

The hard-wall boundary condition requires that $\partial(g^I+g^s)/\partial\rho$ be 0 at $\rho=a$. This gives

$$A_m = -i\pi\epsilon_m\frac{J_m'(\beta a)}{H_m^{(1)'}(\beta a)}H_m^{(1)}(\beta\rho_o)H_m^{(1)}(\beta\rho) \tag{A9}$$

Thus,

$$G(\rho,\phi\mid\rho_o,\phi_o;\beta)i\pi\sum_{m=-\infty}^{\infty}e^{im\phi}\left[J_m(\beta\rho_<) - \frac{J_m'(\beta a)}{H_m^{(1)'}(\beta a)}H_m^{(1)}(\beta\rho_<)\right]H_m^{(1)}(\beta\rho_>) \tag{A10}$$

where $\rho_<$ and $\rho_>$, respectively, represent the smaller and the larger of the values ρ and ρ_o.

Using Watson's transformation [13]

$$G(\rho,\phi\mid\rho_o,\phi_o;\beta) = -\frac{\pi}{2}\oint\frac{e^{i\nu(\phi-\pi)}}{\sin\nu\pi}\times\left[\frac{J_\nu(\beta\rho_<)H_\nu^{(1)'}(\beta a)-J_\nu'(\beta a)H_\nu^{(1)}(\beta\rho_<)}{H_\nu^{(1)'}(\beta a)}\right]H_\nu^{(1)}(\beta\rho_>)\,d\nu \tag{A11}$$

This integral can be closed in both the upper- and lower-half planes for $|\phi|<\pi/2$ (shadow region). Thus the integral can be evaluated by the method of residues:

$$G(\rho,\phi\mid\rho_o,\phi_o;\beta) = \pi^2 i\sum_n\frac{e^{\pm i\nu_n(\phi-\pi)}}{\sin\pm\nu_n\pi}\frac{J_{\pm\nu_n}'(\beta a)}{\partial H_{\pm\nu_n}^{(1)'}(\beta a)/\partial\nu}H_{\pm\nu_n}^{(1)}(\beta\rho_<)H_{\pm\nu_n}^{(1)}(\beta\rho_>) \tag{A12}$$

Note that one of the terms from Eq. (A11) is missing because the residue is evaluated at the zeros of $H_\nu^{(1)'}(\beta a)$. Using the identities (Jones [13], p. 673)

$$H_{-\nu}^{(1)}(z) = e^{\nu\pi i}H_\nu^{(1)}(z) \qquad J_\nu(z) = \frac{1}{2}[H_\nu^{(1)}(z)+H_\nu^{(2)}(z)]$$
$$J_{-\nu}(z) = \frac{1}{2}[e^{\nu\pi i}H_\nu^{(1)}(z)+e^{-\nu\pi i}H_\nu^{(2)}(z)]$$
$$\frac{\partial H_{-\nu}^{(1)}(z)}{\partial\nu} = -e^{\nu\pi i}\frac{\partial H_\nu^{(1)}(z)}{\partial\nu} \tag{A13}$$

it can be shown that

$$G(\rho,\phi\mid\rho_o,\phi_o;\beta) = \pi^2 i\sum_n\frac{\cos\nu_n(\phi-\pi)}{\sin\nu_n\pi}\left[\frac{H_{\nu_n}^{(2)'}(\beta a)}{\partial H_{\nu_n}^{(1)'}(\beta a)/\partial\nu}\right]H_{\nu_n}^{(1)}(\beta\rho_o)H_{\nu_n}^{(1)}(\beta\rho) \tag{A14}$$

Here

$$\nu_n = \beta a+\left(\frac{\beta a}{2}\right)^{1/3}q_n e^{i\pi/3} \tag{A15}$$

$$\frac{H_{\nu_n}^{(2)'}(\beta a)}{\partial H_{\nu_n}^{(1)'}(\beta a)/\partial\nu} = \frac{1}{2\pi}\left(\frac{\beta a}{2}\right)^{1/3}\frac{\exp(i5\pi/6)}{q_n\mathrm{Ai}^2(-q_n)} \tag{A16}$$

where q_n is the nth root of $\mathrm{Ai}'(-q)=0$, Ai being the AiryAi function. For large ν_n,

$$\frac{1}{\sin\nu_n\pi}\sim -2i\exp(i\nu_n\pi) \tag{A17}$$

Hence

$$\frac{\cos\nu_n(\phi-\pi)}{\sin\nu_n\pi}\sim -i[e^{i\nu_n\phi}+e^{i\nu_n(2\pi-\phi)}] \tag{A18}$$

The three-dimensional Green's function can be obtained by taking the inverse Fourier transform:

$$g(\rho,\phi,z\mid\rho_o,\phi_o,z_o) = \frac{1}{2\pi}\int_{-\infty}^{\infty}G(\rho,\phi\mid\rho_o,\phi_o;\sqrt{k^2-\zeta^2})e^{i\zeta(z-z_o)}\,d\zeta \tag{A19}$$

Therefore,

$$g(\boldsymbol{r}\mid\boldsymbol{r_o}) = \frac{1}{4}e^{i5\pi/6}\sum_n\frac{1}{q_n\mathrm{Ai}^2(-q_n)}\int_{-\infty}^{\infty}\left(\frac{\sqrt{k^2-\zeta^2}}{2}a\right)^{1/3}\times H_{\nu_n}^{(1)}(\sqrt{k^2-\zeta^2}\rho_o)H_{\nu_n}^{(1)}(\sqrt{k^2-\zeta^2}\rho)[e^{i\nu_n\phi}+e^{i\nu_n(2\pi-\phi)}]e^{i\zeta(z-z_o)}\,d\zeta \tag{A20}$$

Note that $|\zeta|<|k|$ for propagating waves. Let $\zeta=k\cos\alpha$. Then, because $k\gg 1$,

$$g(\boldsymbol{r}\mid\boldsymbol{r_o}) = \frac{k\sin\alpha}{4}e^{i5\pi/6}\sum_n\frac{1}{q_n\mathrm{Ai}^2(-q_n)}\int_0^{\pi}\left(\frac{ka}{2}\sin\alpha\right)^{1/3}\times H_{\nu_n}^{(1)}(k\rho_o\sin\alpha)H_{\nu_n}^{(1)}(k\rho\sin\alpha)[e^{i\nu_n\phi}+e^{i\nu_n(2\pi-\phi)}]e^{ik\cos\alpha(z-z_o)}\,d\alpha \tag{A21}$$

For large ν and z (see Abramowitz and Stegun [14], p. 368),

$$H_\nu^{(1)}(\nu z)\sim 2e^{-i\pi/3}\left(\frac{4\xi}{1-z^2}\right)^{1/4}\frac{1}{\nu^{1/3}}\mathrm{Ai}(e^{i2\pi/3}\nu^{2/3}\xi) \tag{A22}$$

where

$$\frac{2}{3}(-\xi)^{(3/2)} = \sqrt{z^2-1} - \cos^{-1}\frac{1}{z} \tag{A23}$$

Using the asymptotic expansion of Ai( ), this can be written as

$$H_\nu^{(1)}(\nu z) \sim e^{-i\pi/3}\pi^{-1/2}\nu^{-1/3}\left(\frac{4}{1-z^2}\right)^{1/4} \times (e^{2i\pi/3}\nu^{2/3})^{-1/4}\exp[-2/3(e^{2i\pi/3}\nu^{2/3}\xi)^{3/2}] \tag{A24}$$

$$= \sqrt{\frac{2}{\pi}}\frac{\nu^{-1/2}e^{-i\pi/2}}{(1-z^2)^{1/4}}\exp\left\{-\nu e^{i\pi}\frac{2}{3}[e^{-i\pi}(-\xi)]^{3/2}\right\} \tag{A25}$$

Note that $\arg(-\xi) = 0$, and -1 is written as $\exp(-i\pi)$ inside the square brackets because the modulus of the argument of the AiryAi function should be less than π for the above expansion to be valid. Using the expression for ξ, we get

$$H_\nu^{(1)}(\nu z) \sim \sqrt{\frac{2}{\pi}}\frac{\nu^{-1/2}e^{-i\pi/2}}{(1-z^2)^{1/4}}\exp\left\{i\nu\left[\sqrt{z^2-1} - \cos^{-1}\left(\frac{1}{z}\right)\right]\right\} \tag{A26}$$

substituting, $\nu = \nu_n$ and $\nu z = kr$,

$$H_{\nu_n}^{(1)}(\beta r) \sim \sqrt{\frac{2}{\pi}}\frac{e^{-i\pi/2}}{(\nu_n^2-\beta^2r^2)^{1/4}}\exp\left\{i\nu_n\left[\frac{\sqrt{\beta^2r^2-\nu_n^2}}{\nu_n} - \cos^{-1}\left(\frac{\nu_n}{\beta r}\right)\right]\right\} \tag{A27}$$

Since $\nu_n = \beta a + O(\beta a)^{1/3}$,

$$H_{\nu_n}^{(1)}(\beta r) \sim -i\sqrt{\frac{2}{\pi\beta}}\frac{1}{(a^2-r^2)^{1/4}}\exp\left[i\beta\sqrt{r^2-a^2} - i\nu_n\cos^{-1}\left(\frac{a}{r}\right)\right] \tag{A28}$$

Thus

$$H_{\nu_n}^{(1)}(k\sin\alpha\rho_o)H_{\nu_n}^{(1)}(k\sin\alpha\rho) \sim \frac{-2i}{\pi k\sin\alpha}\frac{1}{(\rho_o^2-a^2)^{1/4}}\frac{1}{(\rho^2-a^2)^{1/4}}\exp\left\{ik\sin\alpha(\sqrt{\rho^2-a^2} + \sqrt{\rho_o^2-a^2}) - i\nu_n\left[\cos^{-1}\left(\frac{a}{\rho}\right) + \cos^{-1}\left(\frac{a}{\rho_o}\right)\right]\right\} \tag{A29}$$

Note that the branch cut is chosen in such a way that

$$\frac{i}{(\rho_o^2-a^2)^{1/4}}\frac{1}{(\rho^2-a^2)^{1/4}} = \frac{1}{(a^2-\rho_o^2)^{1/4}}\frac{1}{(a^2-\rho^2)^{1/4}} \tag{A30}$$

With these approximations, the Green's function can now be written as

$$g(\boldsymbol{r}|\boldsymbol{r_o}) = \frac{e^{i5\pi/6}}{2\pi}\frac{1}{(\rho_o^2-a^2)^{1/4}}\frac{1}{(\rho^2-a^2)^{1/4}}\sum_n\frac{1}{q_n\mathrm{Ai}^2(-q_n)}\int_0^\pi\left(\frac{ka}{2}\sin\alpha\right)^{1/3} \times[e^{i\nu_n\phi} + e^{i\nu_n(2\pi-\phi)}]\exp\left\{ik\sin\alpha(\sqrt{\rho^2-a^2} + \sqrt{\rho_o^2-a^2}) - i\nu_n\left[\cos^{-1}\left(\frac{a}{\rho}\right) + \cos^{-1}\left(\frac{a}{\rho_o}\right)\right]\right\}e^{ik\cos\alpha(z-z_o)}\,\mathrm{d}\alpha \tag{A31}$$

This integral is in the form of $\int \Phi e^{i\Psi}$ and can be evaluated by the method of stationary phase. Neglecting terms of order smaller than ka, the stationary point $\bar{\alpha}$ is given by the root of the equation $\mathrm{d}\Psi/\mathrm{d}\alpha = 0$:

$$\tan\bar{\alpha} = \frac{a}{z-z_o}\left[(\phi-\phi_o) - \cos^{-1}\left(\frac{a}{\rho}\right) - \cos^{-1}\left(\frac{a}{\rho_o}\right) + \frac{\sqrt{\rho^2-a^2}}{a} + \frac{\sqrt{\rho_o^2-a^2}}{a}\right] \tag{A32}$$

Defining z using the helical angle θ as

$$z - z_o = a\left[(\phi-\phi_o) - \cos^{-1}\left(\frac{a}{\rho}\right) - \cos^{-1}\left(\frac{a}{\rho_o}\right) + \frac{\sqrt{\rho^2-a^2}}{a} + \frac{\sqrt{\rho_o^2-a^2}}{a}\right]\Big/\tan\theta \tag{A33}$$

the stationary point is simply

$$\bar{\alpha} = \theta \tag{A34}$$

$$\left.\frac{\mathrm{d}^2\Psi}{\mathrm{d}\alpha^2}\right|_{\alpha=\bar{\alpha}} = -k(z-z_o)/\cos\theta \tag{A35}$$

Hence,

$$g(\boldsymbol{r}\,|\,\boldsymbol{r_o}) = \frac{e^{i\pi/12}}{\sqrt{2\pi}}\frac{1}{(\rho_o^2-a^2)^{1/4}}\frac{1}{(\rho^2-a^2)^{1/4}}\sum_n\frac{1}{q_n\mathrm{Ai}^2(-q_n)}\left(\frac{ka}{2}\sin\theta\right)^{1/3} \times\frac{\sqrt{\cos\theta}}{\sqrt{k(z-z_o)}}[e^{i\nu_n\phi} + e^{i\nu_n(2\pi-\phi)}]\exp\left\{ik\sin\theta(\sqrt{\rho^2-a^2} + \sqrt{\rho_o^2-a^2}) - i\nu_n\left[\cos^{-1}\left(\frac{a}{\rho}\right) + \cos^{-1}\left(\frac{a}{\rho_o}\right)\right]\right\}e^{ik\cos\theta(z-z_o)} \tag{A36}$$

Let

$$a\left[(\phi-\phi_o) - \cos^{-1}\left(\frac{a}{\rho}\right) - \cos^{-1}\left(\frac{a}{\rho_o}\right)\right] = \sigma\sin\theta \tag{A37}$$

Therefore,

$$g(\boldsymbol{r}\,|\,\boldsymbol{r_o}) = \frac{e^{i\pi/12}}{2\sqrt{\pi}}\frac{1}{(\rho_o^2-a^2)^{1/4}}\frac{1}{(\rho^2-a^2)^{1/4}} \times(a\cos\theta)^{1/2}(\sin\theta)^{1/3}\left(\frac{ka}{2}\right)^{-1/6}(z-z_o)^{-1/2}\sum_n\frac{1}{q_n\mathrm{Ai}^2(-q_n)} \times[e^{ik(s_o+\sigma+s)}e^{-\alpha_m\sigma} + e^{ik(s_o+\bar{\sigma}+s)}e^{-\alpha_m\bar{\sigma}}] \tag{A38}$$

Here

$$\alpha_m = \left(\frac{k}{2}\right)^{1/3}(a\mathrm{cosec}^2\theta)^{-2/3}\frac{\sqrt{3}}{2}q_m \tag{A39}$$

Equation (A38) has a physical interpretation in terms of rays. s_o is the distance from the source to the tangent point on the cylinder, σ is the creeping length on the cylinder, and s is the distance from the tangent point, from where the ray leaves the cylinder, to the observer. For each source and observer pair there would be two families of rays, creeping from opposite sides of the cylinder as shown in Fig. 5. $\bar{\sigma}$ represents the creeping length of the other ray.

$$g(\boldsymbol{r}\,|\,\boldsymbol{r_o}) = \frac{e^{i\pi/12}}{\sqrt{2\pi k}}\frac{1}{(\rho_o^2-a^2)^{1/4}}\frac{1}{(\rho^2-a^2)^{1/4}}(\cos\theta)^{1/2}\left(\frac{ka}{2}\sin\theta\right)^{1/3} \times(z-z_o)^{-1/2}\sum_n\frac{1}{q_n\mathrm{Ai}^2(-q_n)}[e^{ik(s_o+\sigma+s)}e^{-\alpha_m\sigma} + e^{ik(s_o+\bar{\sigma}+s)}e^{-\alpha_m\bar{\sigma}}] \tag{A40}$$

Finally, the Green's function can be written as

$$g(\boldsymbol{r}\,|\,\boldsymbol{r}_o) = \frac{e^{i\pi/12}}{\sqrt{2\pi k}}\frac{1}{\sqrt{s}}\frac{1}{\sqrt{s_o}}\frac{1}{\sqrt{s_o+s+\sigma}}\left(\frac{k}{2}a\mathrm{cosec}^2\theta\right)^{1/3}\sum_n \frac{1}{q_n \mathrm{Ai}^2(-q_n)} \times [e^{ik(s_o+\sigma+s)}e^{-\alpha_m\sigma} + e^{ik(s_o+\bar{\sigma}+s)}e^{-\alpha_m\bar{\sigma}}] \quad \text{(A41)}$$

Acknowledgments

This work is supported by Cambridge-MIT Institute (CMI) as part of the "Silent Aircraft Initiative." We are grateful to Jesper Oppelstrup and his group for allowing us access to the GEMS (general electromagnetic solvers) project, sponsored by Vinnova in the Parallel and Scientific Computing (PSCI) Center of Excellence at the Royal Institute of Technology (KTH). We would also like to thank Andrew Faszer for his help with ProEngineer, and Steve Thomas and Matthew Sargeant for providing the CAD models for the various geometries used in this paper.

References

[1] Agarwal, A., and Dowling, A. P., "Low-Frequency Acoustic Shielding by the Silent Aircraft Airframe," AIAA Paper 2005-2996, May 2005.

[2] Keller, J. B., "Geometrical Theory of Diffraction," *Journal of the Optical Society of America*, Vol. 52, No. 2, 1962, pp. 116–130.

[3] Sefi, S., "Architecture and Geometrical Algorithms in MIRA," *Proceedings of EMB01*, Dept. of Scientific Computing, Uppsala Univ., Uppsala, Nov. 2001.

[4] Pierce, A. D., *Acoustics, An Introduction to Its Physical Principles and Applications*, American Institute of Physics, New York, 1994.

[5] Taylor, K., "A Transformation of the Acoustic Equation with Implications for Wind-Tunnel and Low-Speed Flight Tests," *Proceedings of the Royal Society of London A*, Vol. 363, No. 1713, 1978, pp. 271–281.

[6] Jeffery, R. W., and Holbeche, T. A., "Experimental Studies of Noise-Shielding Effects for a Delta-Winged Aircraft," AIAA Paper 75-513, 1975.

[7] Keller, J. B., "Diffraction by an Aperture," *Journal of Applied Physics*, Vol. 28, April 1957, pp. 426–444.

[8] Levy, B., and Keller, J. B., "Diffraction by a Smooth Object," *Communications on Pure and Applied Mathematics*, Vol. 12, April 1959, pp. 159–209.

[9] Sefi, S., "Computational Electromagnetics: Software Development and High Frequency Modeling of Surface Currents on Perfect Conductors," Ph.D. Dissertation, Royal Institute of Technology, KTH, School of Computer Science and Communication, Stockholm, Sweden, Dec. 2005.

[10] Diedrich, A., "The Multidisciplinary Design and Optimization of an Unconventional, Extremely Quiet Transport Aircraft," M.S. Thesis, Department of Aeronautics and Astronautics, MIT, Cambridge, MA, 2005.

[11] Hileman, J., Spakovszky, Z., and Drela, M., "Aerodynamic and Aeroacoustic Three-Dimensional Design for a Silent Aircraft," AIAA Paper 2006-241, Jan. 2006.

[12] Morse, P. M., and Feshbach, H., *Methods of Theoretical Physics*, McGraw–Hill, New York, Vol. 2, 1953.

[13] Jones, D. S., *Acoustic and Electromagnetic Waves*, Oxford University Press, Oxford, England, U.K., 1986.

[14] Abramowitz, M., and Stegun, I. A., *Handbook of Mathematical Functions with Formulas, Graphs, and Mathematical Tables*, Dover, New York, 1974.

R. So
Associate Editor